Engineering Failure Analysis 105 (2019) 896–918

Contents lists available at ScienceDirect

Engineering Failure Analysis

journal homepage: www.elsevier.com/locate/engfailanal

Assessment of progressive collapse potential of special moment resisting RC frames – Experimental and FE study

Hussein M. Elsanadedy[a,*,1], Yousef A. Al-Salloum[a], Tarek H. Almusallam[a], Tuan Ngo[b], Husain Abbas[a]

[a] Chair of Research and Studies in Strengthening and Rehabilitation of Structures, Dept. of Civil Engineering, College of Engineering, King Saud University, P.O. Box 800, Riyadh 11421, Saudi Arabia
[b] Department of Infrastructure Engineering, The University of Melbourne, Melbourne, VIC 3010, Australia

ARTICLE INFO

Keywords:
Progressive collapse
SMRF
Beam-column joint
Column loss scenario
FE modeling

ABSTRACT

The catastrophic collapse of the Twin-towers has further prompted structural engineers to understand and investigate the progressive collapse of multi-story buildings. This paper aims to simulate the response of reinforced concrete (RC) special moment resisting frame (SMRF) assemblies under column-loss scenarios through nonlinear finite element (FE) modeling. Besides the modeling of nonlinear rate dependent material behavior, bond-slip effects at the concrete-to-steel rebar interface have been considered. The FE model was calibrated against a scaled, single-story, two-bay by one-bay, RC SMRF model specimen with reinforcement detailing conforming to ACI 318-11 code. The specimen was tested under a middle column removal scenario. The calibrated FE model was subsequently employed for some parametric studies of interest wherein the effect of different parameters such as: type of assembly, column continuity, development of beam rebars at exterior joints, applied axial loads on columns and beam continuity at exterior joints, on the behavior of SMRF under a middle column removal scenario was studied. A simple procedure is also proposed for the progressive collapse assessment of RC SMRFs caused by sudden column removal.

1. Introduction

Progressive collapse is a chain of local and global failures owing to the local failure of structural members caused by anomalous loads. For inhibiting the progressive collapse of a structure, there should be enough redundancy for the development of an alternative load path, even if a vertical load-carrying element is lost. To avoid progressive collapse, different codes [1–6] require the setup of connecting members, selection of appropriate plans, consideration of load combinations covering column-loss scenarios, and methods of introducing alternate load transfer paths. Some concepts for minimizing the progressive collapse potential in RC structures have also been recently patented [7,8].

The progressive collapse behavior was incorporated in various design codes and guidelines [1–6,9,10] through notional column-loss scenarios, which were based on early progressive collapse incidents reported in the past [11,12]. Significant work has been dedicated to study the progressive collapse behavior of steel and RC structures [11–25]. The contribution of compressive arch and catenary actions to the progressive collapse resistance of steel and RC structures has been recently investigated experimentally and

* Corresponding author.
E-mail address: elsanadedy@yahoo.com (H.M. Elsanadedy).
[1] On leave from Helwan University, Cairo, Egypt.

https://doi.org/10.1016/j.engfailanal.2019.07.045
Received 7 March 2019; Received in revised form 16 July 2019; Accepted 18 July 2019
Available online 19 July 2019
1350-6307/

numerically by some researchers e.g. [26–30]. Choi and Kim [31] demonstrated, through experiments performed on RC beam-column sub-assemblages, the role of seismic reinforcement detailing in resisting progressive collapse through the development of catenary actions in beams. In another experimental study by Yu and Tan [32], the contribution of seismic detailing in resisting the progressive collapse of RC frames was also highlighted. The Compressive Arch Action (CAA) and the catenary action were found to significantly enhance the structural resistance against progressive collapse. Kim and Yu [33] investigated numerically the effect of the amount of flexural and shear reinforcement on the progressive collapse potential of RC moment frames. The flexural reinforcement was shown to enhance the catenary action and the amount of shear reinforcement was responsible for the initiation of the catenary action.

The role of reinforcement detailing in the progressive collapse potential of RC frames was also investigated experimentally by the authors through tests performed at King Saud University [34]. Two types of rebar detailing were used – one conforming to the ordinary moment-resisting frames (OMRF) and the other conforming to special moment-resisting frames (SMRF) [3]. The scaled frames were tested under a column-removal scenario. The experiments gave rise to a better understanding on the role of connections in RC floor systems in terms of mitigating the progressive collapse mechanism.

This paper aims to develop finite element (FE) models for predicting the behavior of RC SMRF assemblies under a column-loss scenario. A high fidelity code, LS-DYNA [35], was used for the development of the FE models. The nonlinear rate dependent behavior of concrete and steel, and bond-slip effects at the concrete-to-steel rebar interface were incorporated. The numerical model was validated using the results for a SMRF specimen that was previously tested by the authors [34]. Some parametric studies of interest were also carried out numerically to investigate the effect of different parameters, viz. type of assembly, column continuity, development of beam rebars at exterior joints, axial load application on columns and beam continuity at exterior joints on the response of SMRF under a column-removal scenario. A simple procedure was also developed to analyze the progressive collapse potential of RC SMRFs due to sudden column removal.

The novelty of this work is created from the investigation of the following research points, which have not been studied before in the literature, concerning the progressive collapse potential of special moment resisting RC frames: (i) effect of bond-slip modeling at rebars-to-concrete interface versus the case of perfect bond assumption; (ii) effect of modeling of RC slabs in the 3D assemblies versus the cases of 3D assemblies without slabs and 2D assemblies; (iii) effect of boundary conditions in terms of beam and column continuity and axial load application at exterior joints; and (iv) suggesting a simple analysis procedure for the progressive collapse evaluation using pushover, capacity and load curves.

2. Experimental program

A single story, two-bay by one-bay RC SMRF scaled specimen, tested by the authors at King Saud University [34] under a column-loss scenario, has been employed for validating the FE model adopted in this study. The test specimen (denoted as SMRF) was designed as a quarter-scale of the exterior bays of a prototype eight-story commercial SMRF building located at a busy intersection of the city of Jeddah in Saudi Arabia. As per the Saudi Building Code SBC 301 requirements [36], the seismic design parameters of the building are: Occupancy Category III, Site Class E and Seismic Design Category C. All spans in the prototype building were 8.0 m. The superimposed dead load and live load used in the design were 2 and 3 kN/m^2, respectively and the building design conformed to both the Saudi Building Code SBC 304 [37] and the ACI 318–11 code [3]. Table 1 provides the building dimensions and reinforcement detailing for both the prototype assembly and the SMRF test specimen. The test specimen dimensions are also depicted in Fig. 1. Specimen SMRF comprises of a single-story RC assembly with 2.0 × 4.0 m floor panels supported on beams (B1-B7). The section dimensions of the columns, as well as the beams, were 200 × 200 mm. The RC columns were supported on steel stubs, which were resting on steel rails that were rigidly connected to strong lab floor (Fig. 2). The base of column C2 was removed to represent the

Table 1
Geometric properties and reinforcement detailing of prototype building and test specimen.

Property	Prototype building	Specimen SMRF
Ground story height[a] (m)	6.75	1.69
Typical story height (m)	5	–
Beam span (m)	8	2
Beam width (mm)	800	200
Beam depth (mm)	800	200
Longitudinal rebars of beams	12ϕ20 (top) + 12ϕ20 (bottom)	2ϕ12 (top) + 2ϕ12 (bottom)
Beam stirrups at middle of span	ϕ12 @ 150 mm c/c (6 branches)	ϕ6 @ 100 mm c/c (2 branches)
Beam stirrups at end	ϕ12 @ 75 mm c/c (6 branches)	ϕ6 @ 50 mm c/c (2 branches)
Width of column section (mm)	800	200
Depth of column section (mm)	800	200
Longitudinal rebars of columns	20ϕ28	4ϕ16
Column ties	ϕ12 @ 75 mm c/c (at ends) ϕ12 @ 150 mm c/c (remaining)	ϕ6 @ 50 mm c/c (at ends) ϕ6 @ 100 mm c/c (remaining)
Clear concrete cover to transverse steel (mm)	40	10
Thickness of slab (mm)	240	60

(continued on next page)

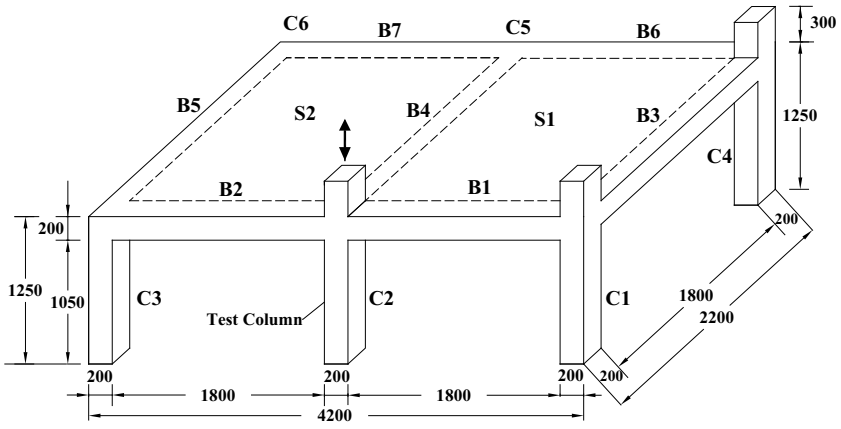

Fig. 1. Concrete dimensions of test specimen SMRF.

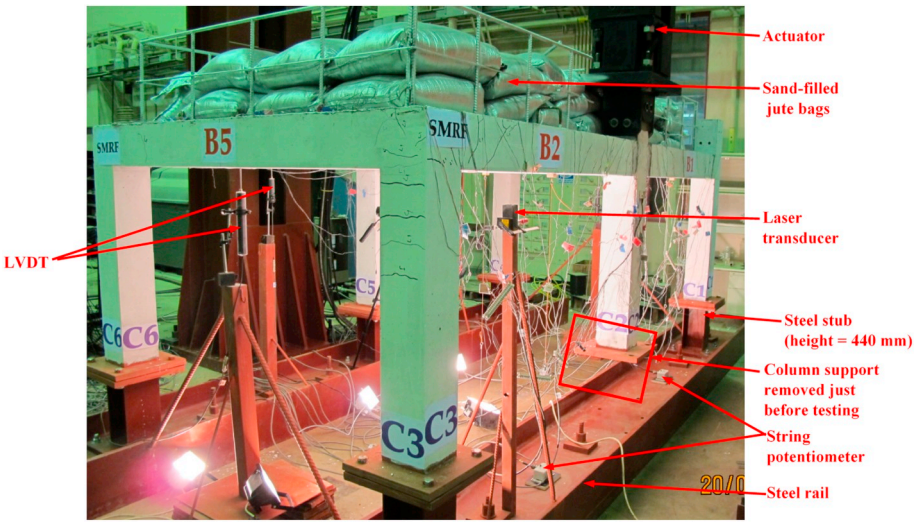

Fig. 2. Instrumented specimen SMRF ready for testing.

column-loss scenario in the case of progressive collapse. This column will be referred to as the “test column” hereafter. Table 2 lists the mechanical properties of concrete and steel rebars measured according to the relevant standards [38,39].

The column removal scenario of the building was simulated by removing the test column support and exerting a suddenly applied load on this column with the help of an actuator with a 1000 kN peak load capacity. The bases of all columns, except the test column, were fixed. The sand-filled jute bags were used for applying a superimposed load of 5 kN/m^2 on the floor slab panels, as shown in Fig. 2.

The data was recorded at a speed of 1 k/s using a high-speed data acquisition system. The rebars of all beams and columns were instrumented with the help of strain gages for recording the strains in the rebars. The vertical displacement of the test column and mid-span displacements of the beams B1, B2 and B4 were measured using string potentiometers and laser transducers. Fig. 2 depicts the instrumentation details of the test specimen.

Fig. 3 shows the displacement-time history applied through the actuator for testing the specimen. Strain rates of the order of 100–10,000 s^{-1} are reported in real progressive collapse scenarios due to blast loads [40]. However, the rate of application of the load in the experiments was 100 mm/s, which was the maximum that could be applied using the actuator. Although the rate of application is on the lower side, the consequent reduction of the inertial loads is expected to be partly compensated by the increase in the material strength due to the strain rate effect. The recorded measurements were analyzed to investigate the mechanism of progressive collapse.

3. FE modeling

The FE analysis of the tested specimen was performed using a general-purpose FE code, namely LS-DYNA [35]. The general-purpose software FEMB Pre-Processor was used to create the FE model. Taking advantage of symmetry, only half of the test specimen was modeled.

Table 2
Material properties used in the FE modeling.

Concrete			
Material model	Type 159 (MAT_CSCM_CONCRETE)		
Density (kg/m^3)	2320		
Uniaxial compressive strength (MPa)	57.3		
Rate effects option, IRATE	1 (Rate effects model turned on)		
Erosion factor, ERODE	1.05		
Pre-existing damage parameter, PRED	0.0 (No pre-existing damage)		
Maximum aggregate size, DAGG (mm)	10.0		
Steel rebars	***ϕ6***	***ϕ12***	***ϕ16***
Material model	Type 24 (MAT_PIECEWISE_LINEAR_PLASTICITY)		
Density (kg/m^3)	7850		
Young's modulus (GPa)	200		
Poisson's ratio	0.3		
Strain rate parameter, *C*	250		
Strain rate parameter, *p*	1.6		
Yield stress (MPa)	290	588	588
Tangent modulus (MPa)	388	660	660
Plastic strain to failure (%)	19.8	14.7	14.7
Steel stubs at base of columns			
Material model	Type 1 (MAT_ELASTIC)		
Density (kg/m^3)	7850		
Young's modulus (GPa)	200		
Poisson's ratio	0.3		

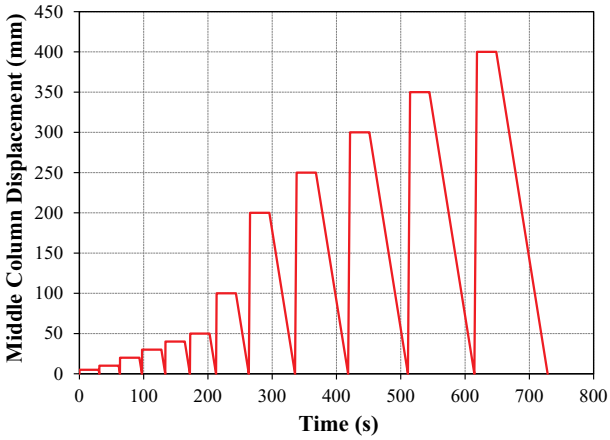

Fig. 3. Typical target displacement-time history for specimen testing.

3.1. Model geometry

Fig. 4(a) and (b) show the FE mesh of the specimen and FE model of the steel rebars, respectively. The concrete volume of the beams, columns and slabs was meshed using eight-node solid hexahedron elements of reduced integration. The Hughes-Liu beam elements were employed for modeling the steel rebars provided in the beams, columns and slabs. Eight-node solid elements were employed for modeling the steel plates and the Belytschko-Tsay shell elements [41] were used to model the I-beams of the steel stubs (Fig. 4(a)).

The size of the concrete mesh in the model was 20 to 30 mm, which was decided based on a mesh sensitivity test. The mesh of the test specimen had 59,352 solid elements of concrete and steel, 11,188 beam elements of steel rebars, and 1120 shell elements of steel.

3.2. Material models

Table 2 presents a summary of the material properties used in the FE modeling. The strain rate sensitivity of the materials was incorporated in the material model because of the dynamic nature of the loads. The continuous surface cap model (type 159) from LS-

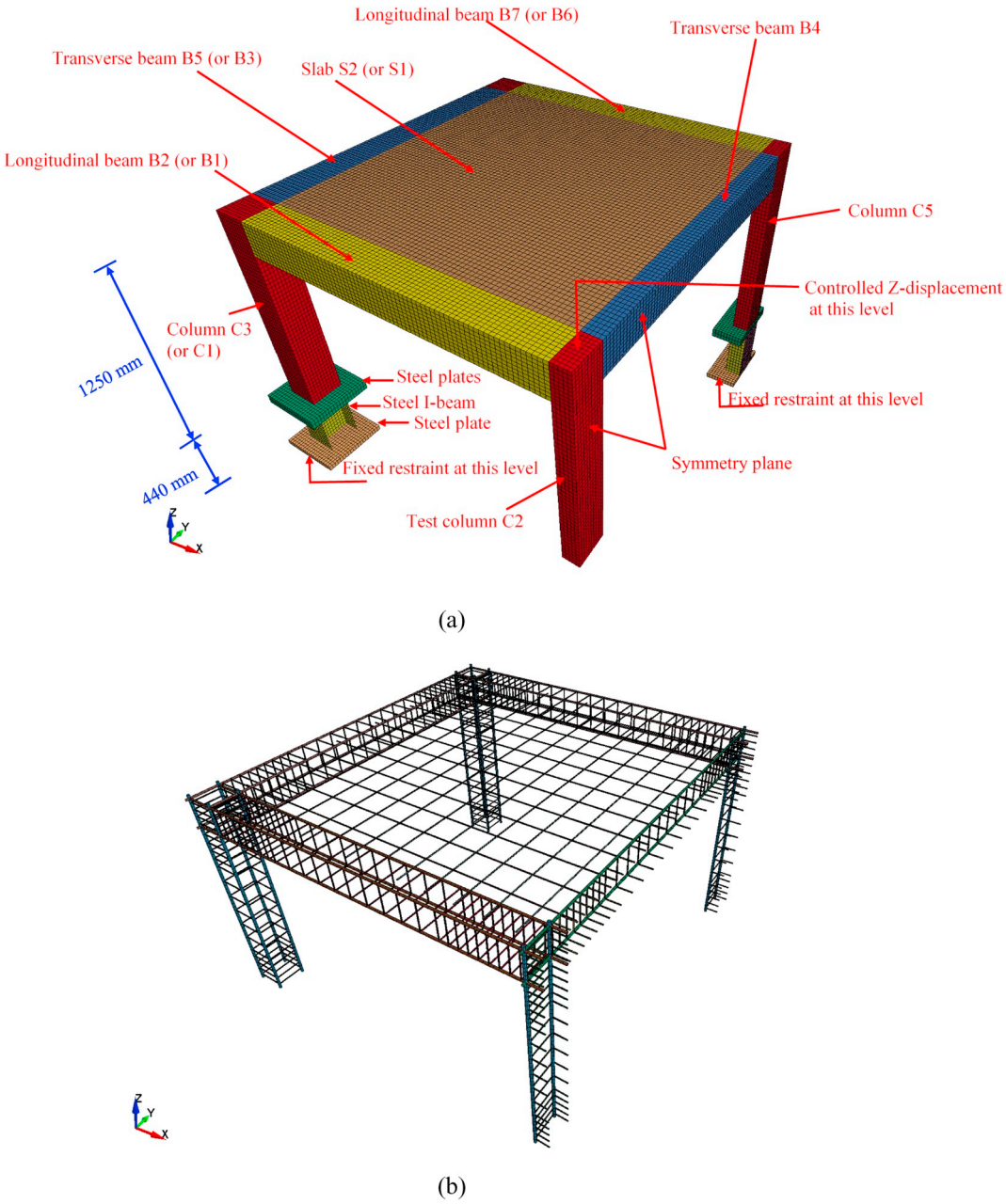

Fig. 4. FE model for specimen SMRF: (a) FE mesh for one-half of specimen; (b) FE model of steel reinforcement for one-half of specimen.

DYNA [35,42] along with the erosion option was used to model the concrete volume. The elasto-plastic material model (type 24) was used for modeling the steel rebars. Cowper-Symonds relation was used to incorporate the enhancement in the yield stress of the steel rebars. The linear elastic material model (type 1) was employed for both the plates and I-beams of the steel stubs.

Based on earlier studies [21,42,43], the erosion of concrete elements was permitted when the principal strain exceeded 0.05. For steel rebars, the plastic tensile strain to failure was employed to activate material erosion.

3.3. Bond-slip effect

In this study, perfect bonding was assumed between the longitudinal and transverse rebars of columns C1 to C6 and surrounding concrete, between the transverse rebars of all beams B1 to B7 and the concrete, and between the main steel rebars of beams B3, B5, B6 and B7 and the concrete. However, bond-slip effects were modeled between the concrete and main rebars of beams B1, B2 and B4, and between the slab rebars and concrete. One-dimensional contact (CONTACT_1D in LS-DYNA) was considered to model the bond

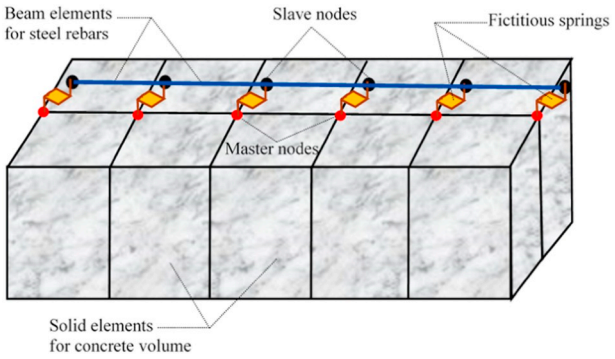

Fig. 5. Sketch of fictitious springs between master and slave nodes in one-dimensional slide line model.

slip between the solid concrete elements and the beam elements of steel rebars through fictitious springs, as shown in Fig. 5 [35].

When the damage accumulation is not considered, the bond between a concrete and steel rebar is assumed to be elastic-perfectly-plastic; when the damage accumulation is considered to be in the plastic range, the bond shear stress will decay exponentially with the increment of plastic slippage. In the elastic range, the bond shear stress, τ, varies linearly with the elastic slip, s ($s < s_{\max}$), up to a maximum value, $\tau_{\max}$, as shown in Fig. 6. The constitutive relation between shear stress and slip is represented by:

$$\tau = \begin{cases} G_s s & s \le s_{\max} \\ \tau_{\max} e^{-h_{\mathrm{dmg}} D} & s > s_{\max} \end{cases} \tag{1}$$

where G_s is the bond shear modulus; $s_{\max}$ is the maximum elastic slip; h_{dmg} is the damage curve exponential coefficient; and D is the damage parameter, which is defined as the sum of the absolute values of the plastic displacement increment Δs_p as

$$D_{n+1} = D_n + \Delta s_p \tag{2}$$

The shear force acting on the bond area per unit length of rebar A_b ($A_b = \pi d_b, d_b$ = rebar diameter)at step $n + 1$ is given as:

$$f_{n+1} = \min(f_n + G_s A_b \Delta s, G_s A_b s_{\max}) \tag{3}$$

According to Eqs. (1) to (3), the typical bond shear stress-slip relationship is shown in Fig. 6.

In order to use the one-dimensional slide line model in LS-DYNA, three parameters are required to be defined. They are the bond shear modulus G_s, the maximum elastic slip $s_{\max}$, and the damage curve exponential coefficient h_{dmg}. In this paper, the maximum elastic slip was taken as 0.254 mm, as recommended by Xiao and Rui [44], and the maximum bond stress $\tau_{\max}$ was assumed as $1.9 f_t$ [45], where f_t is the tensile strength of concrete $= 0.62\sqrt{f_c'}$ (where f_c' = specified compressive strength of concrete in MPa units). Hence, the bond shear modulus G_s was assumed as:

$$G_s = \frac{1.9 \times 0.62\sqrt{f_c'}}{0.254} = 4.64\sqrt{f_c'} \qquad \text{(MPa units)} \tag{4}$$

The damage curve exponential coefficient, h_{dmg}, was taken as a variable in this study, as will be discussed later in Section 4.

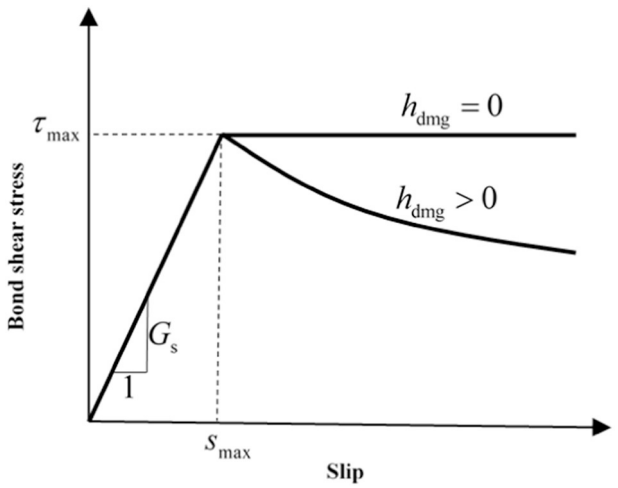

Fig. 6. Bond shear stress-slip relationship for the one-dimensional slide line model.

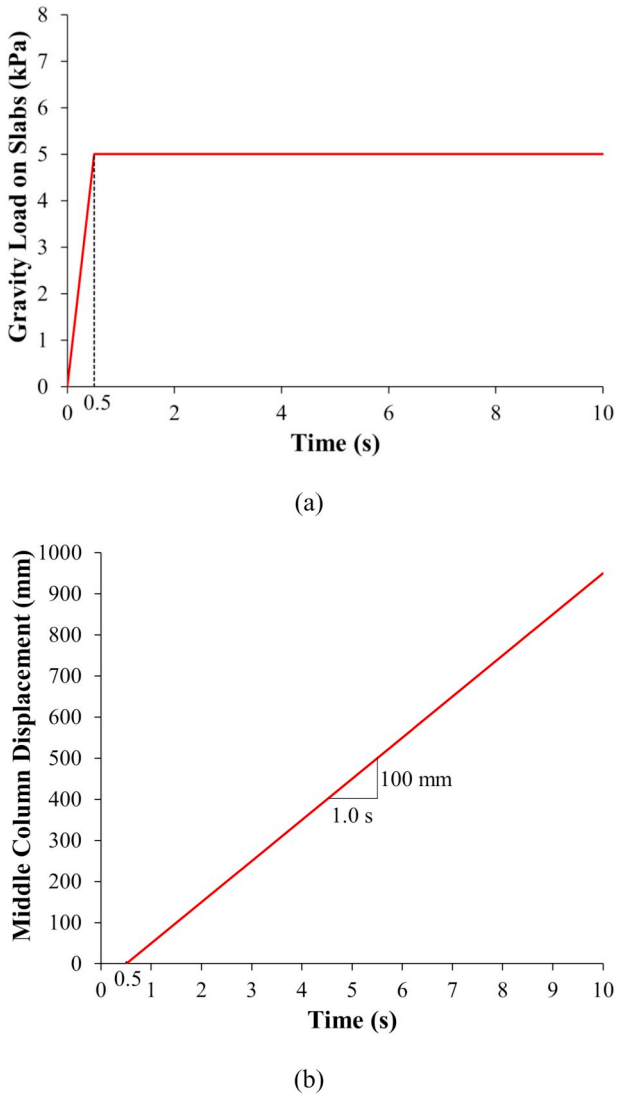

Fig. 7. Load application for FE model of specimen SMRF: (a) Gravity load on slabs; (b) Prescribed vertical displacement at location of middle column C2.

3.4. Loading and boundary conditions

The displacement and rotation of the base of the columns (bottom surface of steel stubs) were restrained in all the three Cartesian directions, as shown in Fig. 4(a). The plane of symmetry was modeled by restraining the global X displacement and the global Y and Z rotations of the nodes lying in the plane. The superimposed gravity load on the slabs was modeled as a uniform load acting in the negative *Z*-direction as a ramp function increasing from zero at the onset of the analysis to its peak value of 5.0 kPa at a time of 0.5 s, and then held constant for the rest of the analysis time, as seen in Fig. 7. This was done to eliminate the oscillatory response associated with the dynamic analysis. To simulate the experiment, the displacement boundary conditions were applied to the nodes lying on the top surface of the test column using the Z-displacement from the displacement-time history of Fig. 3. The prescribed displacement-controlled loading was assumed to start at a time of 0.5 s at which the gravity load reached its peak value.

4. Calibration of FE model

The modeling procedure and the method of numerical analysis were validated using the test results of the scaled model, which are discussed herein.

As mentioned earlier, bond-slip effects between the concrete and main steel rebars of the beams (B1, B2 and B4) and slab panels (S1 and S2) were included in the numerical model, and the damage curve exponential coefficient (h_{dmg}) was varied from 0.05 to 0.15 in a step of 0.05. Thus, four FE models were prepared for the SMRF test specimen. The first case is for bond-slip effects with

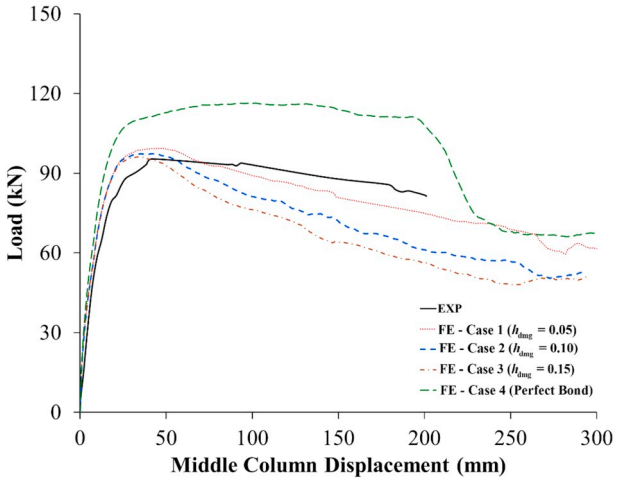

Fig. 8. Comparison of experimental and FE load-displacement envelopes for specimen SMRF.

h_{dmg} = 0.05. The second and third cases are for the curve exponential coefficient (h_{dmg}) of 0.10 and 0.15, respectively. The last case (case 4) is for the analysis with a perfect bonding assumption between all reinforcing bars and concrete, which was taken as an upper bound solution. Fig. 8 shows the comparison between the load-displacement variations obtained from the analysis and the experiments. It can be observed that the perfect bond assumption of case 4 considerably overestimated the stiffness and the peak load i.e. with the ratio of the predicted peak load to that obtained from experiment is 1.22. The FE model of cases 2 and 3 significantly underestimated the post peak load slope of the load-displacement curve. However, the load-displacement curve obtained from the numerical analysis of case 1 closely fits the experiments. Therefore, the bond-slip model with a damage curve exponential coefficient (h_{dmg}) of 0.05 was considered to be successful in estimating the load-displacement characteristics of the SMRF specimen. It should be noted from Fig. 8 that the experimental load-displacement curve did not continue beyond the middle column displacement of about 200 mm because the test was stopped due to the limitation of the actuator stroke.

Figs. 9 and 10 depict the experimental failure modes for the frames and slabs, of the SMRF test specimen, respectively, compared to the predicted failure modes. The FE modes of failure in the figures are shown using damage contours (effective plastic strain) ranging from 0 to 1, with 0 indicating no damage and 1 designating full damage. It should be noted that the experimental failure modes shown in Figs. 9 and 10 were obtained at the end of the test (at middle column displacement of about 200 mm) and the FE failure modes were presented at the same displacement level for the sake of comparison. Due to the limitation of the representation of the smeared crack approach, whereby the cracks are distributed over the elements rather than isolated, the comparison between the crack pattern obtained from the experiment and the damage parameter in the model does not show a precise correlation. The damage parameter appears to be spread over a wider area of damage because the smeared crack approach smears the hairline cracks, which may not be visible in the tests. However, as shown in Figs. 9 and 10, the damage parameter contours obtained from the FE model tend to provide a reasonable estimate of crack growth in the test specimen. As illustrated from Figs. 9 and 10, considerable damage was noted in both slab panels S1 and S2, longitudinal beams B1 and B2 and the transverse beam B4. Columns C1, C2, C3 and C4 were lightly damaged. However, all columns C5 and C6, longitudinal beams B6 and B7 and transverse beams B3 and B5 were almost undamaged. As seen from Fig. 9(a) and (b), plastic hinges were formed in the longitudinal beams B1 and B2 near the zone of their connection with the middle column, which are indicated by wide flexural cracks and concrete crushing in the compression zone (Fig. 9(b)). However, at the exterior joints (near columns C1 and C3), a plastic hinge was not formed in the beam due to partial slippage of the top beam rebars in the joint region, which can be evidenced from the longitudinal splitting cracks at the exterior joints, as displayed in Fig. 9(b). For the transverse frame containing a test column, slippage was also noticed between the bottom rebars of beam B4 and test column C2, and between the top rebars of beam B4 and outer column C5, as seen in Fig. 9(c). Slippage of the rebars of beams B1, B2 and B4 at the exterior joints can be explained as follows:

According to Sec. 12.5 of the ACI 318-11 code [3], the tension development length of deformed rebars terminating in a standard hook (l_{dh}) shall not be less than the largest of $0.24f_y/\sqrt{f_c'}\,d_b$, $8d_b$ and 150 mm, where f_y is the yield strength of the rebars (in MPa); f_c' is the specified compressive strength of concrete (in MPa); and d_b is the rebar diameter (in mm). Hence, for the prototype building, l_{dh} was calculated as 373 mm (for ϕ20 mm rebars) and the available distance for anchorage inside the outer columns was 720 mm, which will provide full development of the beam rebars. However, for the model scale assembly (specimen SMRF), l_{dh} was calculated as 224 mm (for ϕ12 mm rebars) and the available distance for anchorage inside the outer columns was only 168 mm, which will not provide full development of the beam rebars. Accordingly, slippage of the beam rebars occurred at the outer joints as discussed above.

Fig. 10(a) and (b) illustrate the crack pattern observed experimentally for the bottom and top faces of the slabs, respectively, as compared with the damage contours predicted from the FE model at a middle column displacement of 200 mm. A close match could be noticed between the experimental and predicted damage pattern. It is noted that both the experimental and FE crack pattern match the anticipated yield line pattern of slabs having the same boundary and loading conditions.

A comparison between the experimental and FE load-displacement characteristics of the SMRF specimen is listed in Table 3. It is

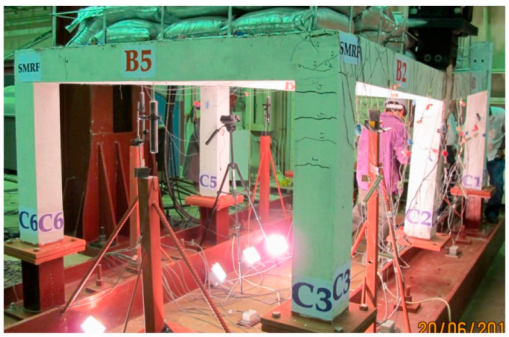

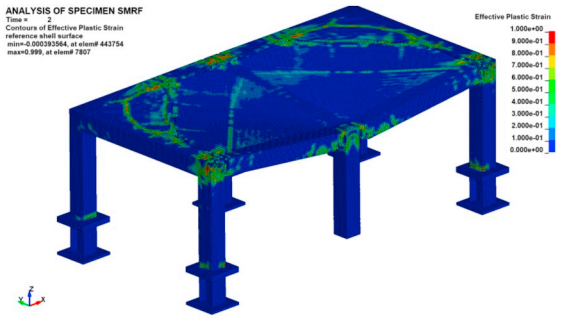

EXP FE

(a)

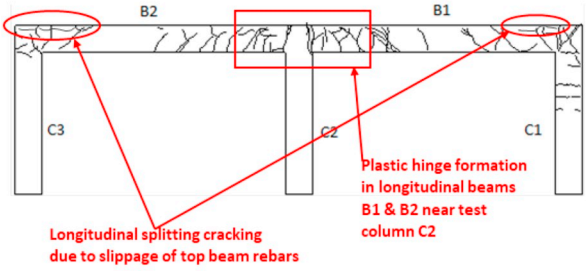

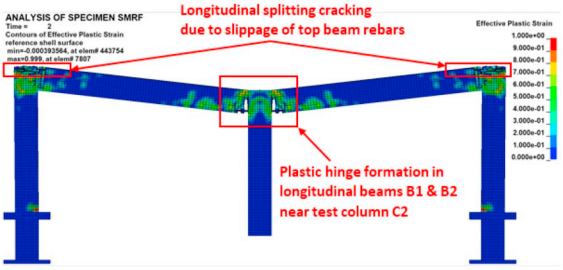

EXP FE

(b)

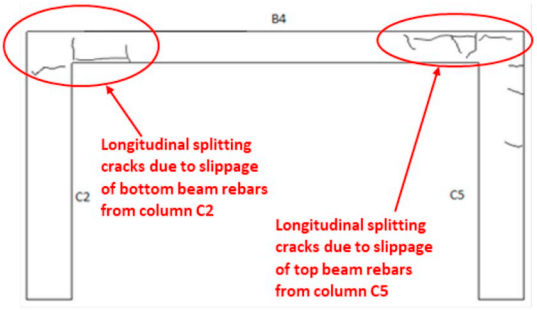

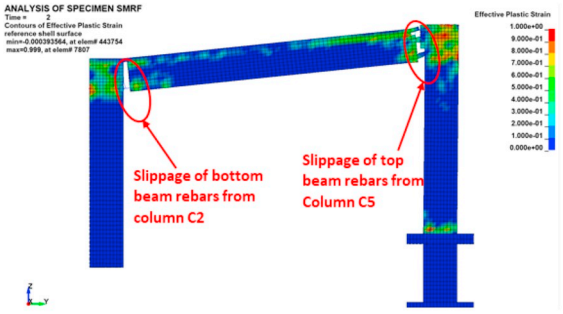

EXP FE

(c)

Fig. 9. Comparison of experimental and FE mode of failure of frames of specimen SMRF: (a) Whole specimen; (b) Longitudinal frame containing test column C2; (c) Transverse frame containing test column C2.

worth mentioning here that the ultimate state used in this study (Table 3) is based on New Zealand Standard-1992 [46], which is defined as the state at which the load in the post peak zone drops to 80% of the peak load. The numerical prediction of the peak load is in close conformity with experiments (Table 3) with a deviation of only 4%. However, compared with the experimental results, deviations of 8%, 10%, 0%, 9% and 2% were observed for the displacement of the test column at the peak load, the displacement of test column at the ultimate state, mid-span displacement of the longitudinal beams B1 & B2 at the ultimate state, mid-span displacement of the transverse beam B4 at the ultimate state and mid-span displacement of the slabs S1 and S2 at the ultimate state, respectively. The energy dissipated at the ultimate state (area under load-displacement curve up to ultimate displacement Δ_u) was predicted efficiently by the FE model with a deviation of 10% (Table 3).

Table 4 shows a comparison between rebar strains obtained numerically and experimentally for the SMRF specimen at ultimate conditions. The numerical values are in close conformity with the experimental values. From Table 4, it is clear that the predicted peak strain for the bottom rebars of longitudinal beams B1 and B2 at the inner column face was about 49 times the rebar yield strain,

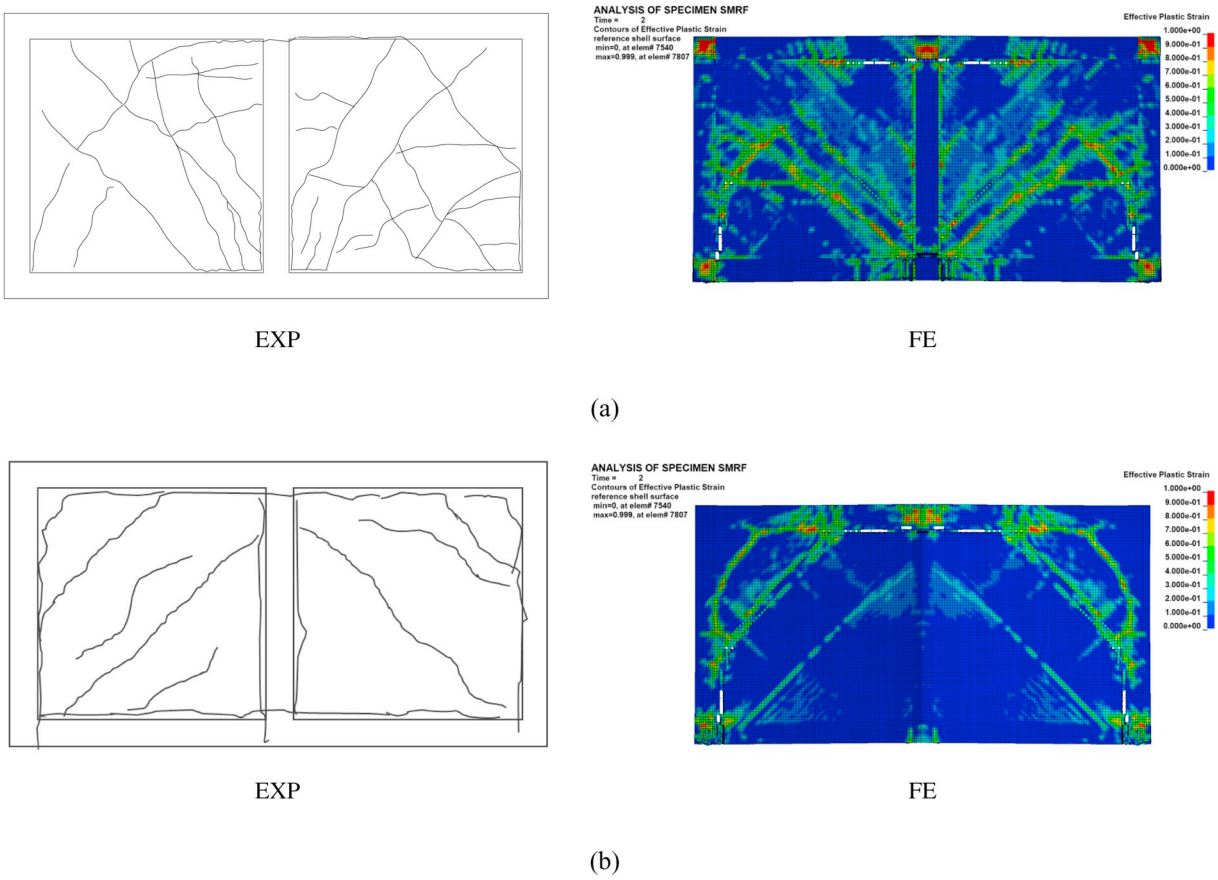

Fig. 10. Comparison of experimental and FE mode of failure of slabs of specimen SMRF: (a) Bottom view; (b) Top view.

Table 3
Comparison of experimental and FE load-displacement characteristics for test specimen SMRF[a].

Results	P_y (kN)	P_u (kN)	Δ_y	$\Delta_{u,c}$	Δ_u	$\Delta_{u,b1,2}$	$\Delta_{u,b4}$	$\Delta_{u,s}$	E_u
			(mm)	(mm)	(mm)	(mm)	(mm)	(mm)	(kNm)
EXP	NA	95.4	NA	41.5	200.6	91.3	87.3	54.8	17.4
FE	73.9	99.4	12.0	45.0	182.6	91.1	96.0	53.6	15.7
EXP/FE	–	0.96	–	0.92	1.10	1.00	0.91	1.02	1.10

[a] P_y = load at first yield of bottom steel rebars of longitudinal beams B1 & B2 at inner column face; P_u = peak load; Δ_y = displacement of middle column C2 at first yield of bottom steel rebars of longitudinal beams B1 & B2; $\Delta_{u,c}$ = displacement of middle column C2 at peak load; Δ_u = displacement of middle column C2 at ultimate state; $\Delta_{u,b1,2}$ = mid-span displacement of longitudinal beams B1 & B2 at ultimate state; $\Delta_{u,b4}$ = mid-span displacement of transverse beam B4 at ultimate state; $\Delta_{u,s}$ = mid-span displacement of slabs S1 & S2 at ultimate state; E_u = energy

which indicates the full formation of plastic hinges as mentioned previously. However, both measured and predicted peak strains for the top rebars of longitudinal beams B1 and B2 at the outer column face were well below the rebar yield strain due to the insufficient development of the top rebars at the outer joints, which caused rebar slippage as discussed earlier. The same behavior was found for the top rebars of transverse beam B4 at the outer column face. Due to the propagation of flexural shear cracks at the ends of both longitudinal beams B1 and B2, and transverse beam B4 (Fig. 9), stirrups at 150 mm from the column face had yielded as indicated from Table 4. As seen in Fig. 10, major cracks occurred diagonally at the exterior corners of slab panels S1 and S2 and hence, high strain values of about 9 and 8 times the rebar yield strain, respectively, were recorded and predicted for the slab rebars located near the exterior corner along the longitudinal direction (Table 4).

5. Parametric study

The validated FE model detailed earlier in Section 3 was further extended to study the effect of different boundary-condition

Table 4
Comparison of experimental and FE strains for test specimen SMRF at ultimate state[a].

Results	Steel rebars of longitudinal beams B1 & B2			Steel rebars of transverse beam B4		Steel rebars of slabs S1 & S2		
	Bottom rebars at inner column face (C2)	Top rebars at outer column face (C1 or C3)	Stirrups at 150 mm from inner column face (C2)	Top rebars at outer column face (C5)	Stirrups at 150 mm from outer column face (C5)	Mid-span along longitudinal direction	Mid-span along transverse direction	Exterior corner along longitudinal direction
EXP	NA	2411	***1755***	2935	***42,746***	928	1218	***13,717***
FE	***144,744***	2386	***1747***	2744	***42,609***	825	1157	***11,553***
EXP/FE	–	1.01	1.00	1.07	1.00	1.13	1.05	1.19

[a] EXP = experimental; FE = finite element; NA = not available data; ***strain values in italic bold font exceed their respective yield strains***.

Table 5
Details of FE matrix used in the parametric study.

Specimen ID	Details
Group-A: 3D assembly with slabs	
SMRF	See Table 1 and Figs. 1 & 2
SMRF-CC	Same as specimen SMRF but with continuous columns (two-story specimens) and columns restrained at 2nd floor level
SMRF-CC-FDBR	Same as SMRF-CC but with longitudinal rebars of beams B1, B2 and B4 to be fully developed at outer columns
SMRF-CC-FDBR-AL	Same as SMRF-CC-FDBR but with axial load applied on top of each column
Group-B: 3D assembly without slabs	
SMRF-NS	Same as SMRF but without slabs
SMRF-NS-CC	Same as specimen SMRF-NS but with continuous columns (two-story specimens) and columns restrained at 2nd floor level
SMRF-NS-CC-FDBR	Same as SMRF-NS-CC but with longitudinal rebars of beams B1, B2 and B4 to be fully developed at outer columns
SMRF-NS-CC-FDBR-AL	Same as SMRF-NS-CC-FDBR but with axial load applied on top of each column
Group-C: 2D assembly	
SMRF-2D	2D assembly of specimen SMRF
SMRF-2D-CC	Same as specimen SMRF-2D but with continuous columns (two-story specimens) and columns restrained at 2nd floor level
SMRF-2D-CC-FDBR	Same as SMRF-2D-CC but with longitudinal rebars of beams B1 and B2 to be fully developed at outer columns
SMRF-2D-CC-FDBR-AL	Same as specimen SMRF-2D-CC-FDBR but with axial load applied on exterior columns
SMRF-2D-CC-FDBR-AL-BC	Same as specimen SMRF-2D-CC-FDBR-AL but with beams B1 and B2 to be continuous after exterior columns (4-span assembly)

parameters on the behavior of a SMRF assembly under a middle column-removal scenario. Including the SMRF specimen, the matrix for parametric analysis consisted of 13 specimens with different parameters, viz. type of assembly, column continuity at the exterior joints, development of beam rebars at the exterior joints, axial load application on top of the columns, and beam continuity at the exterior joints (see Table 5). The FE mesh for representative specimens used in the parametric study is presented in Fig. 11. It should be noted that in the designation of specimens used in the parametric analysis, the acronyms “NS” and “2D” stand for no slab and 2D assembly, respectively, the acronym “CC” denotes continuous columns at exterior joints (i.e. two-story specimens), the acronym “FDBR” symbolizes fully developed beam rebars at exterior joints, the acronym “AL” stands for axial load application on top of the columns, and the acronym “BC” stands for continuous beams at exterior joints. As illustrated in Table 5, three different groups of specimens were investigated. In the first group (Group-A), 3D assemblies comprising seven beams, six columns and two slabs were studied for sudden removal of the middle column of the outer longitudinal frame (see Fig. 11(a)). In the second group of specimens (Group-B), 3D assemblies without slabs (comprising seven beams and six columns as seen in Fig. 11(b)) were analyzed. However, the third group of specimens (Group-C) comprised of 2D assemblies as seen in Table 5 and Fig. 11(c) and (d). The first specimen of each group (specimens SMRF, SMRF-NS and SMRF-2D) is a single story without axial load applied on columns and the rebars of the beams are not fully developed in tension at the outer joints as discussed previously. The second specimen of each group is the same as the first specimen but with continuous columns at exterior joints (two-story specimens). The columns of the second story were restrained at their top 200-mm length (representing beams traversing the column) against translation in the global X and Y directions, and against rotation about the global X, Y and Z directions as seen in Fig. 11(a). The third specimen of each group is the same as the second specimen but with longitudinal rebars of beams B1, B2 and B4 (for groups A and B) and beams B1 and B2 (for group C) to be fully developed in tension at the exterior joints. This was done numerically by assuming perfect bonding at the rebar-to-concrete interface for nodes lying only beyond the centerline of the outer columns. However, for the rest of the rebar nodes, bond-slip effects were considered as detailed previously in Section 3. The fourth specimen of each group is the same as the third specimen but with the application of an axial load on top of columns of the second story level (see Fig. 11(b) to (d)). In order to estimate the amount of axial load applied on the columns of model-scale specimens, a 3D FE model was created for the eight-story prototype building using ETABS software [47] with the inclusion of all structural members (beams, columns and slabs) and different load cases (self-weight, superimposed dead and live loads). The axial load ratio on the columns of the second story of the prototype building at the service load level was calculated. The axial load on the columns of the model-scale specimens was then assessed and applied on the top nodes of the columns as a ramp function increasing from zero at the onset of the analysis to its peak value at a time of 0.5 s, and then held constant for the rest of the analysis time (similar to the gravity load on slabs shown in Fig. 7(a)). The effect of beam continuity after the exterior joints was only studied for the 2D assembly as seen in Table 5. Specimen SMRF-2D-CC-FDBR-AL-BC is the same as specimen SMRF-2D-CC-FDBR-AL but with continuous beams at the end joints (4-span assembly) as seen in Fig. 11(d).

Table 6 provides a summary of the results of numerical analysis of 13 specimens. The results are given in terms of all response parameters at both different stages and the ultimate state. The FE mode of failure for the representative samples of 3D and 2D assemblies used in the parametric study are also depicted in Figs. 12 and 13, respectively. Fig. 14(a) to (c) show comparisons between the load versus middle column displacement envelopes obtained from the FE model of specimens from groups A to C, respectively. The evolution of axial force in the beam for the five 2D assemblies used in the parametric study is also presented in Fig. 15. It is clear that neither the compressive arch action (CAA) nor catenary action (CA) was developed for single-story specimens due to the insufficient restraint provided by the outer columns and also due to the inadequate tension development of the top beam rebars inside the outer joints. This was also evidenced from Fig. 15 for the axial force in the beams of specimen SMRF-2D, which was very small (close to zero) for the whole displacement history of the specimen. For single-story specimens, flexural action was only developed at the inner beam-column joints of the longitudinal beam via plastic hinge formation. However, it was not developed at the outer joints due to rebar slippage as depicted from the strains reported in Table 6 for the top beam rebars, which were well below their respective

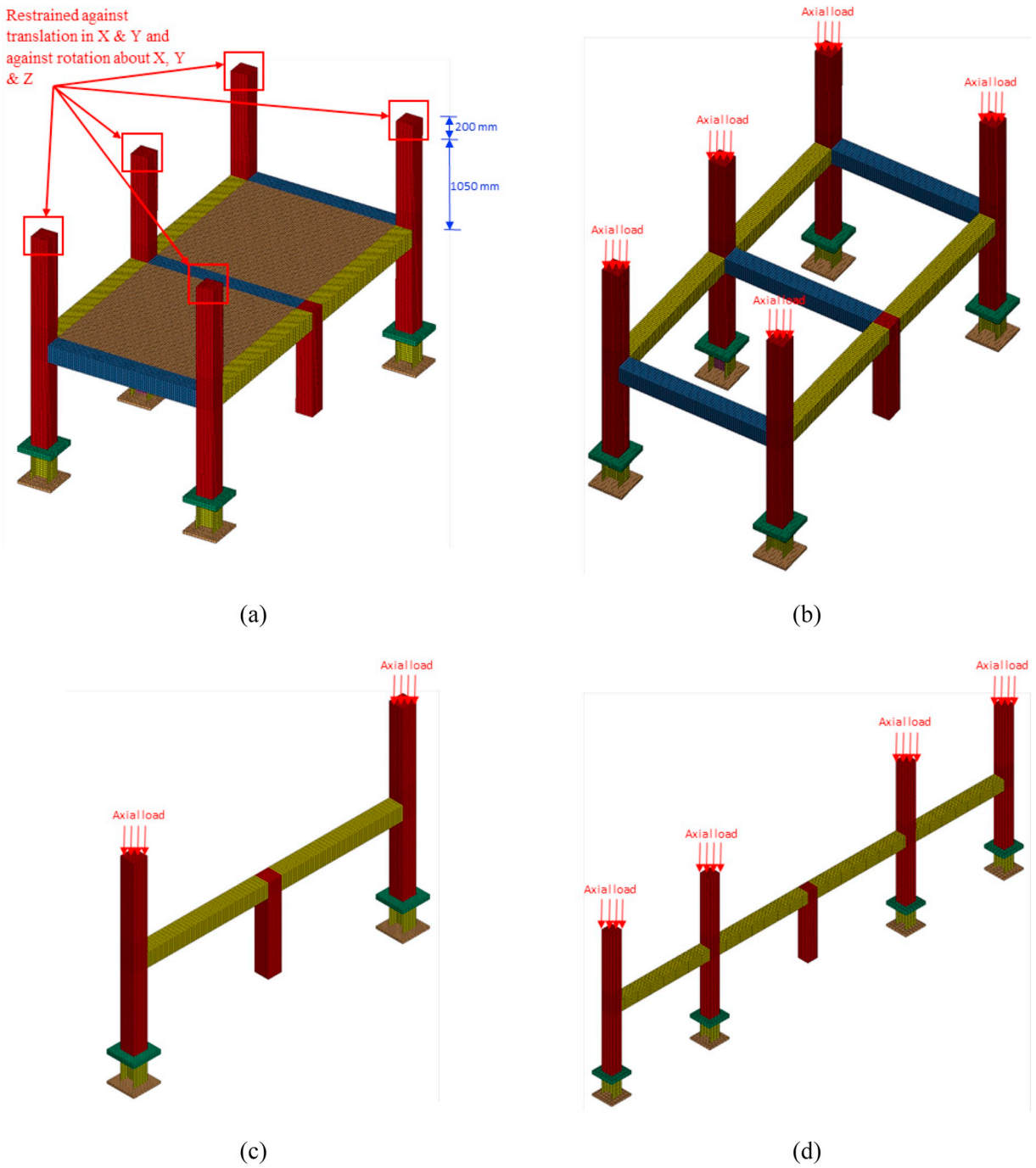

Fig. 11. FE mesh for representative specimens used in the parametric study: (a) Specimen SMRF-CC-FDBR; (b) Specimen SMRF-NS-CC-FDBR-AL; (c) Specimen SMRF-2D-CC-FDBR-AL; (d) Specimen SMRF-2D-CC-FDBR-AL-BC.

yield value. For two-story specimens (having continuous columns at exterior joints) with an insufficient development length of beam rebars inside outer columns, both flexural and catenary actions were partially developed as seen from Table 6 and Figs. 12, 14 and 15. However, a compressive arch action was not developed for these specimens as the compressive axial force in longitudinal beams of specimen SMRF-2D-CC was 79 kN (3.4% of the beam axial capacity). This value was considerably less than 10% of the axial beam capacity, which as per the ACI 318–11 code [3], would not affect the flexural capacity, and could thereby be ignored. For two-story specimens with a full development of beam rebars at the exterior joints, both flexural and catenary actions were fully developed as seen in Table 6 and Figs. 12 to 15. However, a compressive arch action (CAA) was not developed as the peak compressive axial force of the beam of specimen SMRF-2D-CC-FDBR was only 72 kN (3.1% of the axial beam capacity). Also, for the two-story specimens with

Table 6
Summary of FE results for all specimens[a].

Specimen ID	Flexural action stage						Compressive arch action stage			
	Development	P_y (kN)	Δ_y (mm)	$P_{u,FA}$ (kN)	$\Delta_{u,c\text{-}FA}$ (mm)	$N_{u,FA}$ (kN)	Development	$P_{u,CAA}$ (kN)	$\Delta_{u,c\text{-}CAA}$ (mm)	$N_{u,CAA}$ (kN)
Group-A: 3D assembly with slabs										
SMRF	P	74	12	99	45	−28	N	–	–	–
SMRF-CC	P	75	12	103	60	−251	N	–	–	–
SMRF-CC-FDBR	F	78	12	116	116	−236	N	–	–	–
SMRF-CC-FDBR-AL	F	98	12	146	101	−371	N	–	–	–
Group-B: 3D assembly without slabs										
SMRF-NS	P	55	13	72	29	−22	N	–	–	–
SMRF-NS-CC	P	57	13	76	31	−177	N	–	–	–
SMRF-NS-CC-FDBR	F	65	15	86	60	−164	N	–	–	–
SMRF-NS-CC-FDBR-AL	F	75	13	103	57	−124	N	–	–	–
Group-C: 2D assembly										
SMRF-2D	P	36	14	41	38	−16	N	–	–	–
SMRF-2D-CC	P	39	13	53	48	−79	N	–	–	–
SMRF-2D-CC-FDBR	F	41	13	62	95	−72	N	–	–	–
SMRF-2D-CC-FDBR-AL	F	51	14	72	73	−117	N	–	–	–
SMRF-2D-CC-FDBR-AL-BC	F	64	15	89	46	−229	F	82	97	−238

Specimen ID	Catenary action stage					$\varepsilon_{b,u}$ (με)	$\varepsilon_{t,u}$ (με)	Δ_u (mm)	E_u (kN.m)	P_u (kN)
	Development	$P_{u,CA}$ (kN)	$P_{u,CA}$ / $P_{u,FA}$	$\Delta_{u,c\text{-}CA}$ (mm)	$N_{u,CA}$ (kN)					
Group-A: 3D assembly with slabs										
SMRF	N	–		–	–	***144,744***	2386	183	15.7	99
SMRF-CC	P	110	1.08	454	142	***196,927***	2336	514	48.5	110
SMRF-CC-FDBR	F	152	1.31	698	208	***205,156***	***182,347***	712	83.1	152
SMRF-CC-FDBR-AL	F	229	1.57	740	229	***209,582***	***172,228***	763	115.8	229
Group-B: 3D assembly without slabs										
SMRF-NS	N	–		–	–	***139,136***	2345	105	6.4	72
SMRF-NS-CC	P	69	0.91	445	241	***202,600***	2368	504	28.6	76
SMRF-NS-CC-FDBR	F	138	1.61	898	293	***233,859***	***234,699***	912	89.2	138
SMRF-NS-CC-FDBR-AL	F	203	1.96	798	209	***226,521***	***201,343***	800	105.1	203
Group-C: 2D assembly										
SMRF-2D	N	–		–	–	***138,351***	1673	100	3.6	41
SMRF-2D-CC	P	63	1.19	479	103	***199,336***	2227	494	22.3	63
SMRF-2D-CC-FDBR	F	90	1.46	504	113	***225,307***	***174,850***	607	41.6	90
SMRF-2D-CC-FDBR-AL	F	126	1.74	510	186	***222,795***	***175,454***	566	46.5	126
SMRF-2D-CC-FDBR-AL-BC	F	269	3.01	888	274	***213,274***	***198,505***	889	129.9	269

[a] P = partially developed; N = not developed; F = fully developed; P_y = load at first yield of bottom steel rebars of longitudinal beams B1 & B2 at inner column face; Δ_y = displacement of middle column C2 at first yield of bottom steel rebars of longitudinal beams B1 & B2; $P_{u,FA}$ = peak load of flexural action stage; $\Delta_{u,c\text{-}FA}$ = displacement of middle column C2 at peak load of flexural action stage; $N_{u,FA}$ = peak floor axial force at flexural action stage (+ve is tension); $P_{u,CAA}$ = peak load of compressive arch action stage; $\Delta_{u,c\text{-}CAA}$ = displacement of middle column C2 at peak load of compressive arch action stage; $N_{u,CAA}$ = peak floor axial force at compressive arch action stage (+ve is tension); $P_{u,CA}$ = peak load of catenary action stage; $\Delta_{u,c\text{-}CA}$ = displacement of middle column C2 at peak load of catenary action stage; $N_{u,CA}$ = peak floor axial force at catenary action stage (+ve is tension); $\varepsilon_{b,u}$ = strain of bottom steel rebars of longitudinal beams B1 & B2 at inner column face at ultimate state; $\varepsilon_{t,u}$ = strain of top steel rebars of longitudinal beams B1 & B2 at outer column face at ultimate state; Δ_u = displacement of middle column C2 at ultimate state; E_u = energy dissipated at ultimate state; P_u = progressive collapse resistance = maximum of $P_{u,FA}$, $P_{u,CAA}$ and $P_{u,CA}$; ***strain values in italic bold font exceed their respective yield strains***.

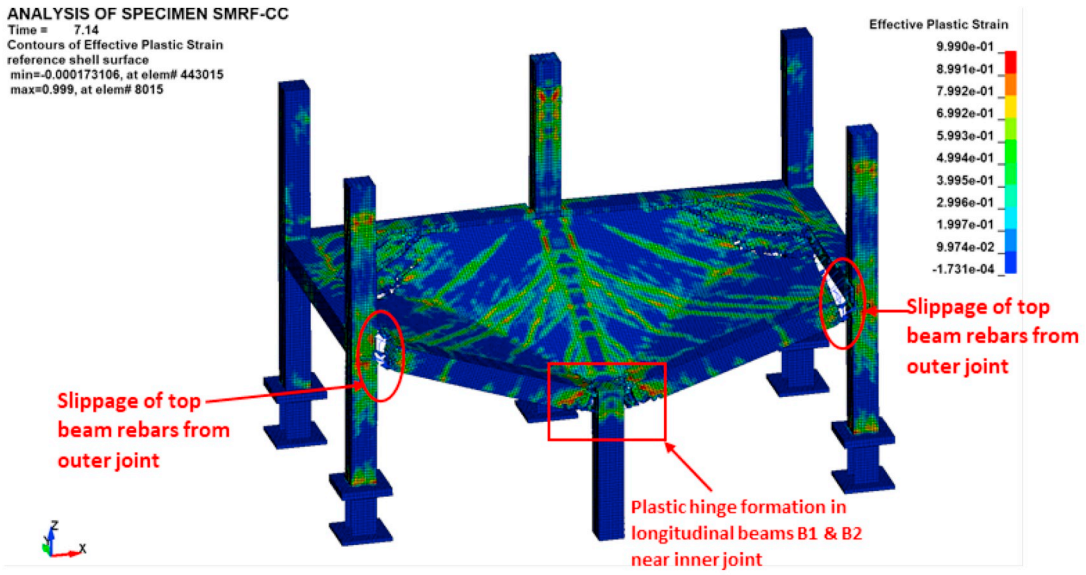

(a)

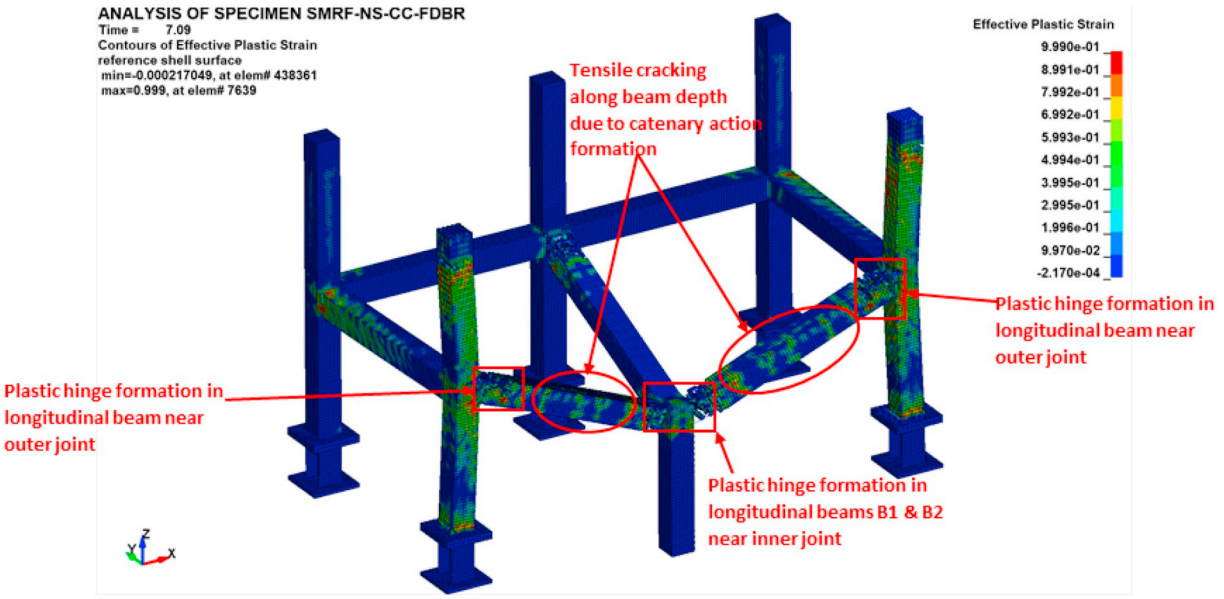

(b)

Fig. 12. FE mode of failure for representative 3D assemblies used in the parametric study: (a) Specimen SMRF-CC; (b) Specimen SMRF-NS-CC-FDBR.

fully developed beam rebars at the exterior joints and the applied axial force on top of the columns, both flexural and catenary actions were fully formed. However, the peak axial compression force in the beam of specimen SMRF-2D-CC-FEBR-AL was limited to 5.1% of the beam axial capacity, which shows the absence of the compressive arch action (Fig. 15). In the 2D assembly SMRF-2D-CC-FDBR-AL-BC (having column continuity at the exterior joints, the adequate development of beam rebars at the outer columns, the applied axial load on top of the columns and continuous beams at exterior joints), all action stages were developed as seen in Figs. 13 to 16. Fig. 16 presents the evolution of both the vertical load and beam axial force over the displacement history for specimen SMRF-2D-CC-FDBR-AL-BC. The peak axial compression force in the beams was about 238 kN (10.4% of its axial capacity), which as per the ACI 318–11 code [3], would marginally induce a compressive arch mechanism, as seen in Fig. 16. Also, a catenary action was very clearly developed for this assembly as the axial force changed its sign from compression to tension at a displacement of 139 mm and increased to a peak tensile force of 274 kN (corresponding to the yielding of all beam rebars along the full beam span). This tensile force was almost maintained until a large displacement of 889 mm at which the peak load of 269 kN was attained.

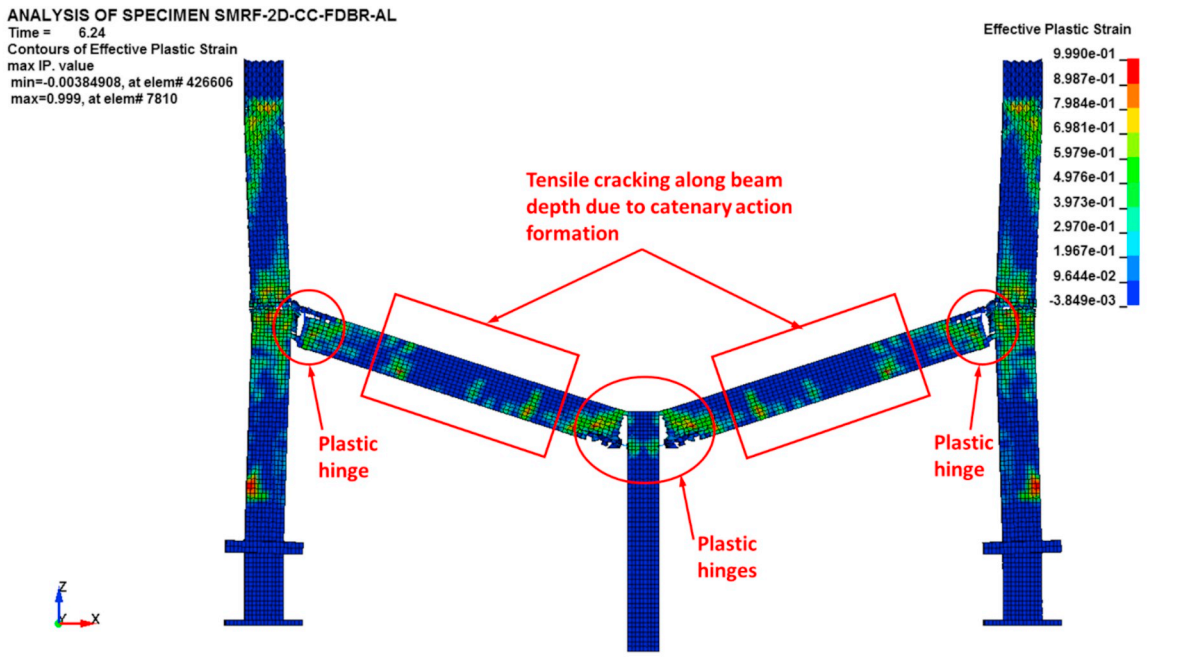

(a)

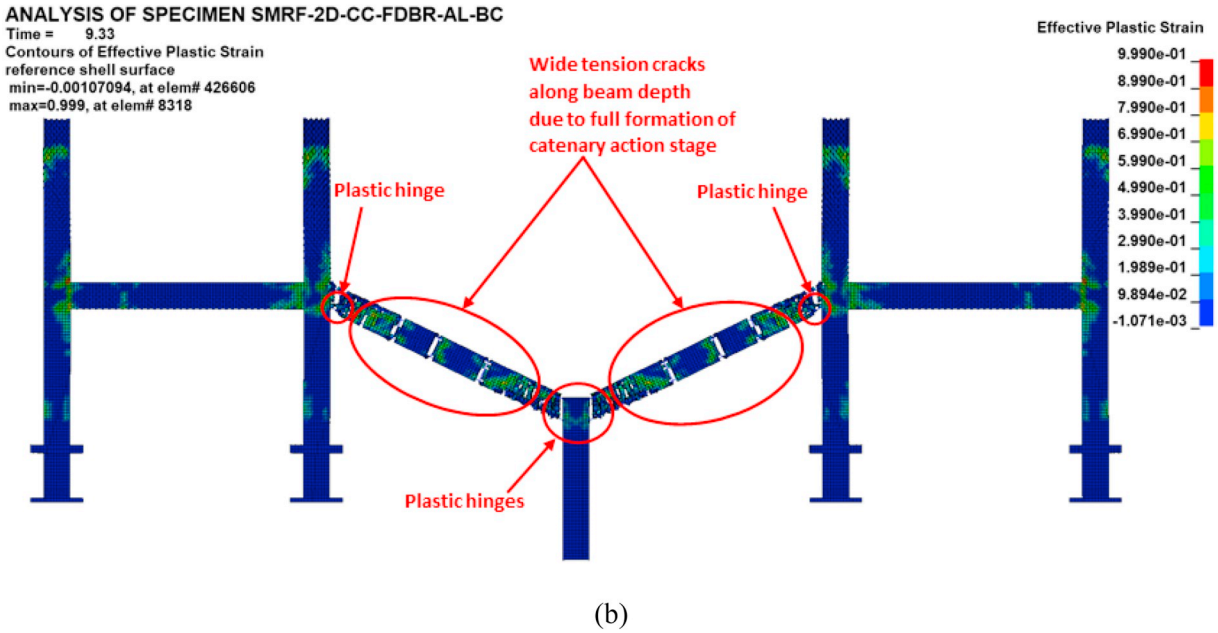

(b)

Fig. 13. FE mode of failure for representative 2D assemblies used in the parametric study: (a) Specimen SMRF-2D-CC-FDBR-AL; (b) Specimen SMRF-2D-CC-FDBR-AL-BC.

In order study the effect of the different boundary-condition parameters on the performance of the numerically investigated specimens, the percentage enhancement in the response parameter was calculated and then plotted for each assembly type, as seen in Figs. 17 to 20. Fig. 17 depicts the effect of column continuity on enhancing the flexural action capacity, progressive collapse resistance and energy dissipated for each assembly type. It is clear from the figure that extending the columns in the FE model to the

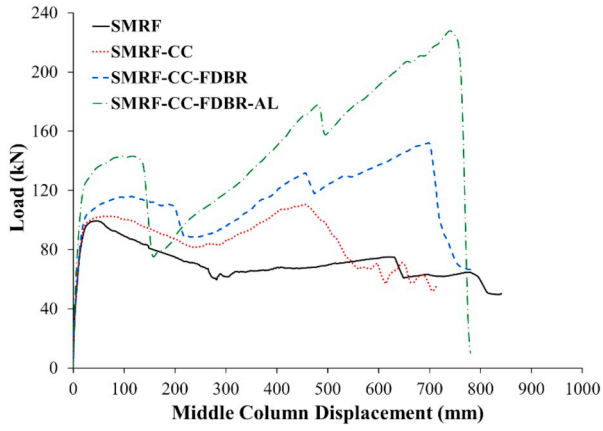

(a)

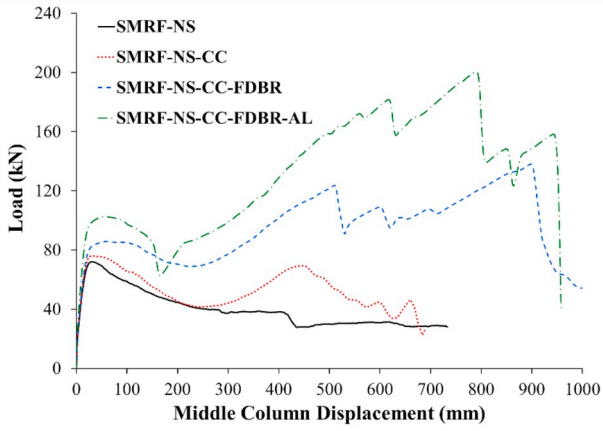

(b)

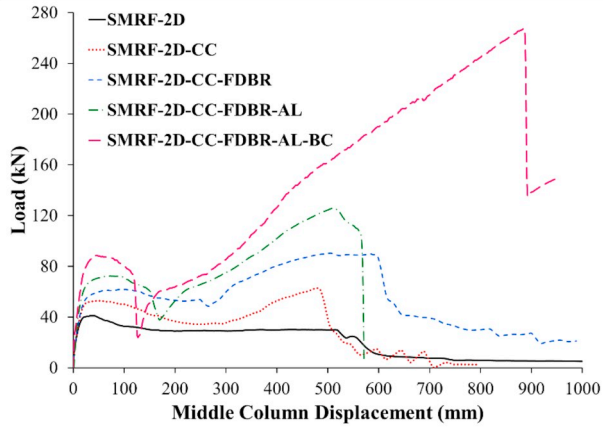

(c)

Fig. 14. Load-displacement envelopes (based on FE analysis) for: (a) Group-A specimens; (b) Group-B specimens; (c) Group-C specimens.

second story level in specimens SMRF-CC, SMRF-NS-CC and SMRF-2D-CC enhanced the flexural action capacity by 3% to 29%, the progressive collapse resistance by 6% to 53% and the energy dissipated at ultimate conditions by 209% to 525% over that of their counterparts SMRF, SMRF-NS and SMRF-2D. The enhancement was more pronounced in the 2D assembly. Continuity of the columns added more restraint to the exterior joints and thereby helped to form the catenary action, which increase the progressive collapse resistance (collapse limit state). Depicted in Fig. 18 is the effect of providing adequate development of the beam rebars at the exterior

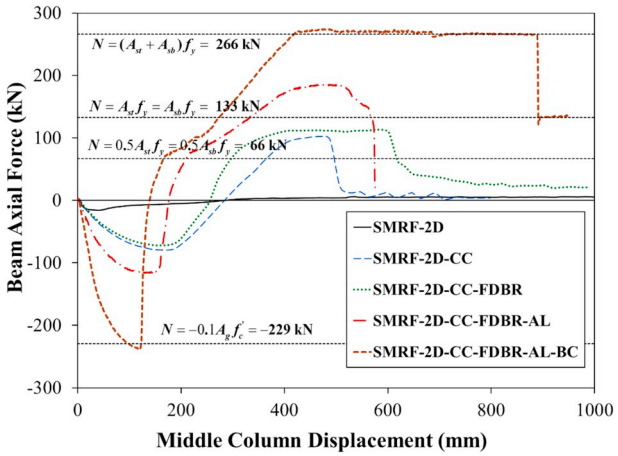

Fig. 15. Evolution of beam axial force for 2D assemblies used in the parametric study.

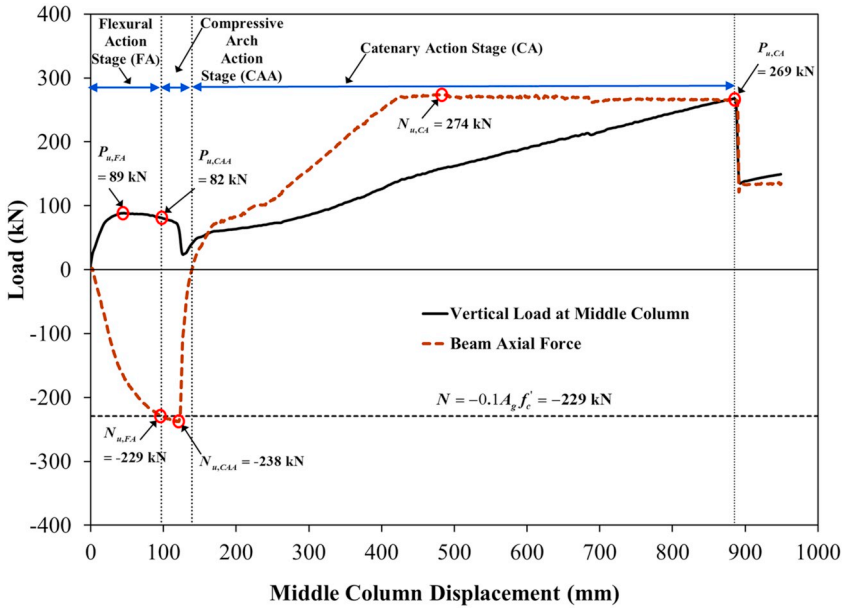

Fig. 16. Development of different action stages for specimen SMRF-2D-CC-FDBR-AL-BC.

joints on the response parameters. This enhancement was calculated for specimens SMRF-CC-FDBR, SMRF-NS-CC-FDBR and SMRF-2D-CC-FDBR with respect to their counterparts SMRF-CC, SMRF-NS-CC and SMRF-2D-CC. It is clear from Fig. 18 that the enhancement in progressive collapse resistance and energy dissipated was clearer for the 3D assembly without a slab (SMRF-NS-CC-FDB) than the other two specimens. The enhancement of the progressive collapse resistance and energy dissipated ranged from 38% to 81% and 71% to 213%, respectively. The enhancement was due to sufficient anchorage provided for the beam rebars at the outer joints, which helped to develop plastic hinges in the beams at the outer columns (see Figs. 12 and 13), and provided sufficient restraint for beams at the outer joints so that catenary action was fully developed as discussed earlier. Fig. 19 illustrates the effect of the axial load application on top of the columns on the response parameters of specimens SMRF-CC-FDBR-AL, SMRF-NS-CC-FDBR-AL and SMRF-2D-CC-FDBR-AL, compared with their counterparts SMRF-CC-FDBR, SMRF-NS-CC-FDBR and SMRF-2D-CC-FDBR. It is clear that the enhancement is more obvious for the 3D assembly with slabs (SMRF-CC-FDBR-AL) than the other two specimens, and the enhancement ranges from 17% to 26%, 39% to 51% and 12% to 39% for the flexural action capacity, progressive collapse resistance and energy dissipated at ultimate state, respectively. Applying an axial load increased the flexural stiffness of the columns and thereby induced more restraint at the outer joints, which increased both flexural and catenary action capacities. Presented in Fig. 20 is the effect of beam continuity at end joints on the performance of the 2D assembly SMRF-2D-CC-FDBR-AL-BC with respect to its counterpart SMRF-2D-CC-FDBR-AL. Since extending the beams beyond the outer joints would increase the redundancy in the load path and add more restraint at the joint, enhancements of 23%, 114% and 179% were calculated for the flexural action capacity, progressive collapse resistance and energy dissipated, respectively, as seen in Fig. 20.

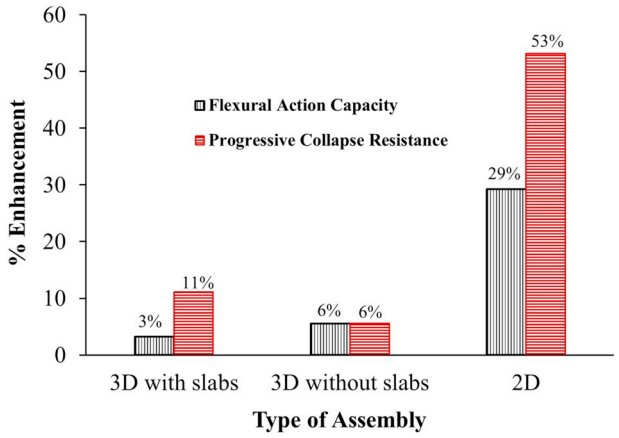

(a)

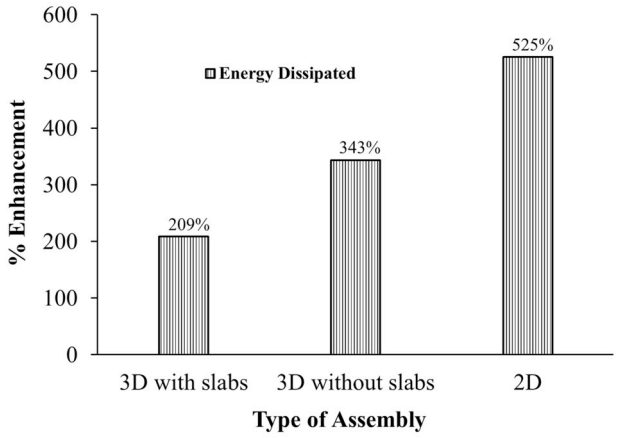

(b)

Fig. 17. Effect of column continuity on enhancement of: (a) Flexural action capacity and progressive collapse resistance; (b) Energy dissipated.

6. Progressive collapse assessment

In a study by Guo and Gilsanz [48], a simple analysis procedure was proposed for the progressive collapse evaluation of 2D RC frames. This procedure was extended in this study for progressive collapse assessment of 3D SMRFs. The first step is to generate a 3D FE model for the whole building using ETABS software [47] and then calculate the reaction of the removed column at the service load level. This reaction was scaled down to represent the model-scale assembly used in this study. The corresponding reaction of the removed column of the quarter-scale 3D assembly was estimated to be about 130 kN. From Table 6, it is clear that the best flexural action performance in terms of yield and peak loads was provided by specimen SMRF-CC-FDBR-AL. Hence, the load-displacement curve of specimen SMRF-CC-FDBR-AL shown in Fig. 14(a) was used as the pushover curve of the structure. According to Guo and Gilsanz [48], if the reaction of the removed column was less than 50% of the yield strength of the pushover curve, the structural frame has low potential for progressive collapse. This condition was not satisfied as the reaction force of the removed column was estimated as 130 kN, which is considerably greater than 50% of the yield strength of the pushover curve ($0.5 \times 98 = 49$ kN). However, if the reaction was larger than the peak strength of the pushover curve, the structural frame has high potential for progressive collapse. This condition was also not met as the reaction force of 130 kN was considerably less than the maximum strength of the pushover curve (229 kN). If the above two conditions are not satisfied, the capacity curve of the structure should be generated and then compared with the load curve. The three curves of the 3D assembly were generated and then plotted, as shown in Fig. 21. The pushover curve is the load-displacement envelope of specimen SMRF-CC-FDBR-AL. The area under the pushover curve gives the amount of energy that the structure can absorb. If the energy below the pushover curve is divided by the corresponding displacement,

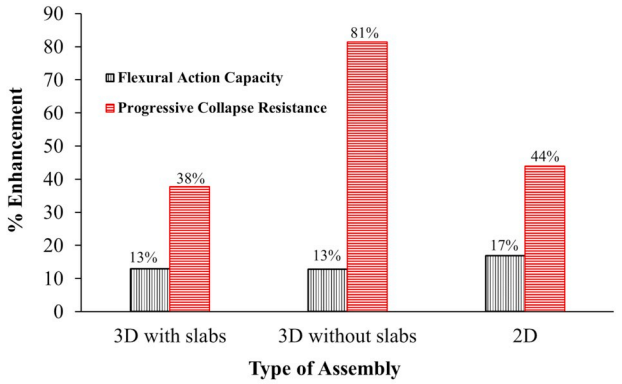

(a)

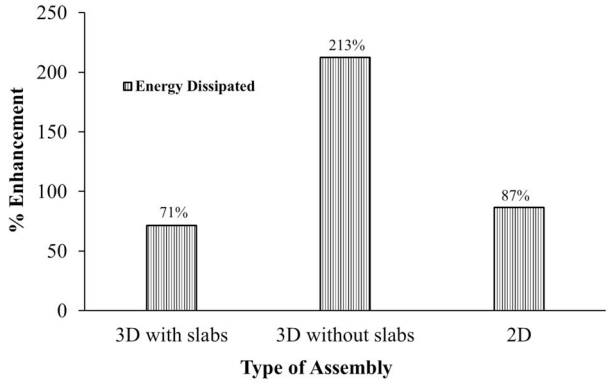

(b)

Fig. 18. Effect of provision of adequate development of beam rebars at exterior joints on enhancement of: (a) Flexural action capacity and progressive collapse resistance; (b) Energy dissipated.

the capacity curve of the structure can be obtained. The load curve is straight in this case and the load corresponds to the reaction of the removed column (130 kN). Fig. 21 shows that before point F, the capacity curve is lower than the load curve. This indicates that before reaching the displacement corresponding to point F (135 mm), the structure cannot absorb the potential energy. It is evident that the structure will collapse if the deflection is corresponding to point F (135 mm), even if the energy can be balanced at point F. Thus, the 3D SMRF has a moderate potential for progressive collapse.

7. Conclusions

The conclusions derived from this study can be summarized as follows:

1. The FE modeling used in this study was found appropriate for assessing the progressive collapse resistance of RC special moment resisting frames. This demonstrates the validity of the FE modeling approach that may be reliably employed in future research on the progressive collapse assessment of RC intermediate moment resisting frame structures due to sudden column-loss scenarios.
2. The assumption of perfect bonding between rebars and concrete overestimates the progressive collapse resistance of RC assemblies subjected to sudden column removal. For the proper prediction of progressive collapse resistance, bond-slip effects have to be modeled at least between concrete and the longitudinal rebars of beams and slabs connected to the removed column.
3. Modeling of RC slabs in the 3D assemblies significantly increased the flexural action capacity and the progressive collapse resistance over 3D assemblies without slabs. Testing and modeling of 3D assemblies with slabs provide a better approximation for progressive collapse resistance under sudden column-loss scenarios, whereas, the 2D assemblies will give lower-bound solutions.
4. The catenary action stage was not developed in assemblies of either single-story or having beams with inadequate development of longitudinal rebars at the outer joints. Column continuity and the provision of full development of beam rebars at the exterior joints favor the full development of both flexural and catenary actions.

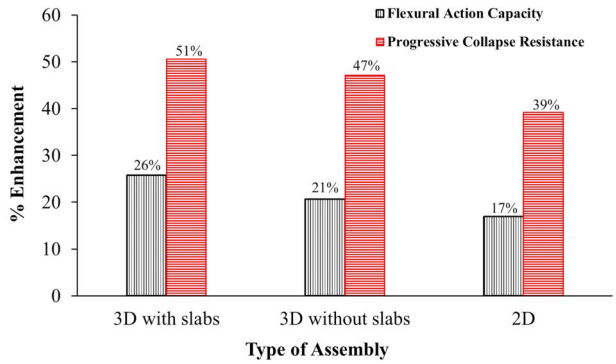

(a)

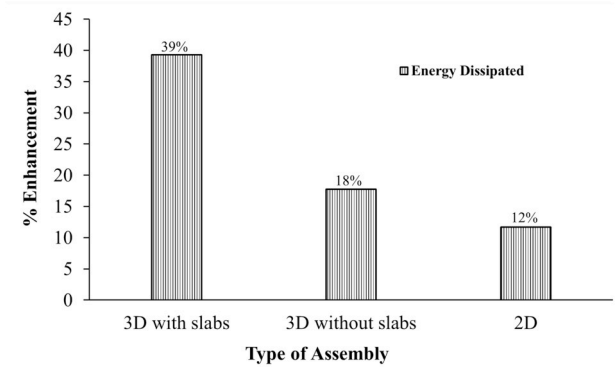

(b)

Fig. 19. Effect of axial load application on top of columns on enhancement of: (a) Flexural action capacity and progressive collapse resistance; (b) Energy dissipated.

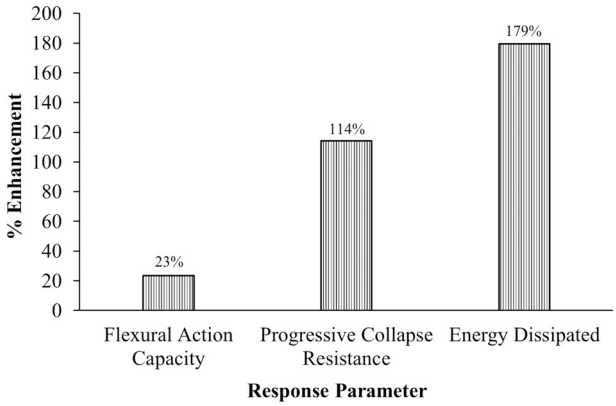

Fig. 20. Effect of beam continuity at exterior joints on enhancement of performance of 2D assembly.

5. Applying an axial load on the columns will increase the flexural stiffness of the columns and thereby induce more restraint at the exterior joints, which would increase both flexural and catenary action capacities. Testing and modeling of RC assemblies without the application of axial loads on columns will then give a lower-bound solution for progressive collapse resistance under abrupt column-removal scenarios.
6. Extending the RC beams beyond the outer joints of the beam-column assembly would increase the redundancy in the load path and add more restraint at the joint, which will in turn enhance the progressive collapse resistance of the assembly under sudden column-loss scenarios.
7. A simple analysis procedure was proposed in this study for the progressive collapse evaluation of 3D RC special moment resisting

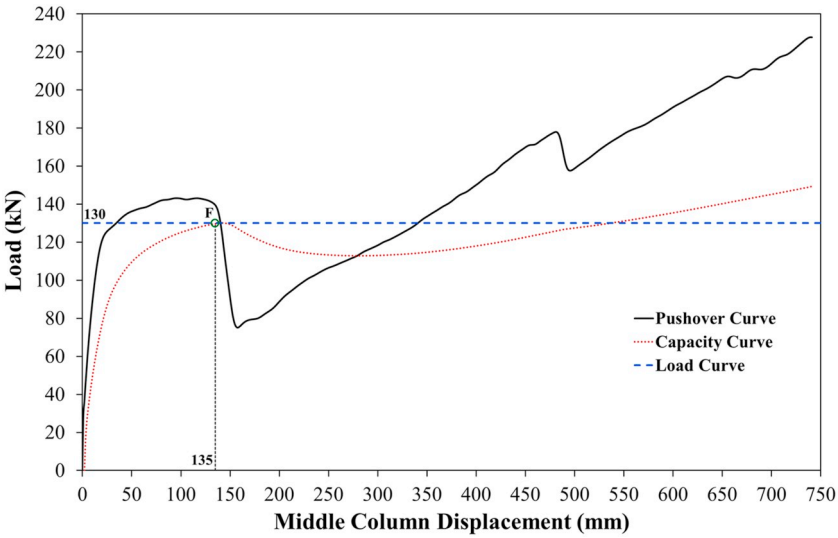

Fig. 21. Progressive collapse assessment using pushover, capacity and load curves.

frames using pushover, capacity and load curves. Based on this procedure, the 3D RC SMRF studied in this research was found to have a moderate potential for progressive collapse.

Declaration of Competing Interest

None.

Acknowledgements

The project was supported by Deanship of Scientific Research Chairs, Saudi Arabia at King Saud University, Saudi Arabia for Chair of Research and Studies in Strengthening and Rehabilitation of Structures at Civil Engineering Department.

References

[1] NRCC (National Research Council of Canada), National Building Code of Canada, National Research Council of Canada, Ottawa, Canada, 1995.
[2] CEN (European Committee for Standardization), Eurocode 1, Actions on Structures, European Committee for Standardization, Brussels, Belgium, 2002.
[3] ACI Committee 318, Building Code Requirements for Structural Concrete and Commentary. ACI 318–11, American Concrete Institute, Detroit, MI, USA, 2011.
[4] ASCE (American Society of Civil Engineers), Minimum Design Loads and Associated Criteria for Buildings and Other Structures (ASCE/SEI 7–16), American Society of Civil Engineers, Reston, Virginia, USA, 2016.
[5] GSA (General Service Administration), Alternate Path Analysis & Design Guidelines for Progressive Collapse Resistance, The U.S. General Services Administration, 2013.
[6] DOD (Department of defense), Unified Facilities Criteria, Design of Building to Resist Progressive Collapse, Department of Defense, U.S, 2005.
[7] H. Abbas, Y.A. Al-Salloum, T.H. Almusallam, Precast Reinforced Concrete Construction Elements with Pre-Stressing Connectors, US patent: US9765521 B1 (19 Sep 2017).
[8] Zheng et al., Reinforced structure for resisting progressive collapse of existing concrete structure, Chinese Patent: CN 203230191 U, 9 Oct 2013.
[9] IBC. International building code, International Code Council, Inc. International Conference of Building Officials, Whittier, CA, 2000, p. 2000.
[10] ISC, ISC security criteria for new federal office buildings and major modernization projects, The Interagency Security Committee, 2001.
[11] C. Pearson, N. Delatte, Ronan point apartment tower collapse and its effect on building codes, J. Perform. Constr. Facil. 19 (2) (2005) 172–177.
[12] T.H. Almusallam, H.M. Elsanadedy, H. Abbas, S.H. Alsayed, Y.A. Al-Salloum, Progressive collapse analysis of a RC building subjected to blast loads, Struct. Eng. Mech, Techno Press 36 (3) (2010) 301–319.
[13] T.H. Almusallam, H.M. Elsanadedy, H. Abbas, P. Mendis, T. Ngo, Numerical analysis for progressive collapse potential of a typical framed concrete building, Int. J. Civ. Environ. Eng. 10 (2) (2010) 40–46 http://www.ijens.org/107002-8989%20IJCEE-IJENS.pdf.
[14] Y.A. Al-Salloum, T.H. Almusallam, M.Y. Khawaji, T. Ngo, H.M. Elsanadedy, H. Abbas, Progressive collapse analysis of RC buildings against internal blast, Adv. Struct. Eng. 18 (12) (2015) 2181–2192.
[15] H.M. Elsanadedy, T.H. Almusallam, Y.R. Alharbi, Y.A. Al-Salloum, H. Abbas, Progressive collapse potential of a typical steel building due to blast attacks, J. Constr. Steel Res. 101 (2014) 143–157.
[16] B.R. Ellingwood, Mitigating risk from abnormal loads and progressive collapse, J. Perform. Constr. Facil. 20 (4) (2006) 315–323.
[17] J. Kim, T. Kim, Assessment of progressive collapse resisting capacity of steel moment frames, J. Constr. Steel Res. 65 (1) (2009) 169–179.
[18] Y. Liu, L. Xu, D.E. Grierson, Compound-element modeling accounting for semi-rigid connections and member plasticity, Eng. Struct. 30 (5) (2008) 1292–1307.
[19] S. Marjanishvili, E. Agnew, Comparison of various procedures for progressive collapse analysis, J. Perform. Constr. Facil. 20 (4) (2006) 365–374.
[20] M.-H. Tsai, B.-H. Lin, Investigation of progressive collapse resistance and inelastic response for an earthquake resistant RC building subjected to column failure, Eng. Struct. 30 (12) (2008) 3619–3628.
[21] H.M. Elsanadedy, T.H. Almusallam, Y.A. Al-Salloum, H. Abbas, Investigation of precast RC beam-column assemblies under column-loss scenario, Constr. Build. Mater. 142 (2017) 552–571.
[22] Y.A. Al-Salloum, H. Abbas, T.H. Almusallam, T. Ngo, P. Mendis, Progressive collapse analysis of a typical RC high-rise tower, J. King Saud Univ. – Eng. Sci. 29 (4) (2017) 313–320.

[23] Y.A. Al-Salloum, M.A. Alrubaidi, H.M. Elsanadedy, T.H. Almusallam, R.A. Iqbal, Strengthening of precast RC beam-column connections for progressive collapse mitigation using bolted steel plates, Eng. Struct. 161 (2018) 146–160.
[24] S. Elkoly, B. El-Ariss, Progressive collapse evaluation of externally mitigated reinforced concrete beams, Eng. Fail. Anal. 40 (2014) 33–47.
[25] S. Li, S. Shan, C. Zhai, L. Xie, Experimental and numerical study on progressive collapse process of RC frames with full-height infill walls, Eng. Fail. Anal. 59 (2016) 57–68.
[26] J. Kim, D. An, Evaluation of progressive collapse potential of steel moment frames considering catenary action, Struct. Des. Tall. Spec. Build 18 (4) (2009) 455–465.
[27] D. Milner, J. Gran, D. Lawver, D. Vaughan, W. Vanadit-Ellis, H. Levine, FLEX analysis and scaled testing for prediction of progressive collapse, First International Workshop on Performance, Protection & Strengthening of Structures under Extreme Loading (PROTECT 2007), Whistler, Canada, 2007.
[28] M. Sasani, J. Kropelnicki, Progressive collapse analysis of an RC structure, Struct. Des. Tall. Spec. Build 17 (4) (2008) 757–771.
[29] W.-J. Yi, Q.-F. He, Y. Xiao, S.K. Kunnath, Experimental study on progressive collapse-resistant behavior of reinforced concrete frame structures, ACI Struct. J. 105 (4) (2008) 433–439.
[30] M. Sasani, M. Bazan, S. Sagiroglu, Experimental and analytical progressive collapse evaluation of actual reinforced concrete structure, ACI Struct. J. 104 (6) (2007) 731–739.
[31] H. Choi, J. Kim, Progressive collapse-resisting capacity of reinforced concrete beam-column sub-assemblage, Mag. Concr. Res. 63 (4) (2010) 297–310.
[32] J. Yu, K.-H. Tan, Experimental and numerical investigation on progressive collapse resistance of reinforced concrete beam column sub-assemblages, Eng. Struct. 55 (2013) 90–106.
[33] J. Kim, J. Yu, Analysis of reinforced concrete frames subjected to column loss, Mag. Concr. Res. 64 (1) (2012) 21–33.
[34] T. Almusallam, Y. Al-Salloum, T. Ngo, P. Mendis, H. Abbas, Experimental investigation of progressive collapse potential of ordinary and special moment resisting reinforced concrete frames, Mater. Struct. 50 (2017) 137.
[35] Livermore Software Technology Corporation (LSTC), LS-DYNA User's Keyword Manual (Nonlinear Dynamic Analysis of Structures in Three Dimensions), Vol. 1 LSTC, Livermore, CA, 2007 Version 971.
[36] Saudi Building Code National Committee (SBCNC), Loads & Forces Requirements—SBC 301. Saudi Arabia, (2007).
[37] Saudi Building Code National Committee (SBCNC), Concrete structures requirements—SBC 304. Saudi Arabia, (2007).
[38] ASTM, Standard test method for compressive strength of cylindrical concrete specimens. ASTM C39/C39M, American Society for Testing and Materials, West Conshohocken, PA, USA, 2010.
[39] ASTM, Standard test methods for tension testing of metallic materials. ASTM E8/E8M, American Society for Testing and Materials, West Conshohocken, PA, USA, 2009.
[40] T. Ngo, P. Mendis, A. Gupta, J. Ramsay, Blast loading and blast effects on structures – An overview, Electron. J. Struct. Eng. (EJSE) Spec. Issue Loading Struct. (2007) 76–91.
[41] T.B. Belytschko, C.S. Tsay, Explicit algorithms for non-linear dynamics of shells, J. Appl. Mech. Appl. Mech. Div. ASME 48 (1981) 209–231.
[42] Y.D. Murray, A. Abu-Odeh, R. Bligh, Evaluation of concrete material model 159, Report No. FHWA-HRT-05-063, US Department of Transportation, Federal Highway Administration National Transportation Systems Center, USA, 2007.
[43] H.M. Elsanadedy, T.H. Almusallam, S.H. Alsayed, Y.A. Al-Salloum, Flexural strengthening of RC beams using textile reinforced mortar – experimental and numerical study, Compos. Struct. 97 (2013) 40–55.
[44] Y. Xiao, M. Rui, Seismic retrofit of RC circular columns using prefabricated composite jacketing, J. Struct. Eng. ASCE 123 (10) (1997) 1357–1364.
[45] F.C. de Witte, User's Manual – Release 9, TNO DIANA BV, Delft, the Netherlands, 2005.
[46] NZS 4203, New Zealand Standard, Code of Practice for General Structural Design and Design Loadings for Buildings 1, (1992), p. 1992.
[47] Computers and Structures, Inc. ETABS, 16.2.0 – Extended 3D Analysis of Building Systems, CSI, Berkeley, CA, USA, 2016, p. 2016.
[48] W. Guo, R. Gilsanz, Simple nonlinear static analysis procedure for progressive collapse evaluation, Proceedings of Blast and Progressive Collapse Symposium, AISC, 2003, pp. 97–106 http://www.emergencymgt.net/sitebuildercontent/sitebuilderfiles/simpleNonlinear.pdf.